First-principles study on structural, vibrational, elastic, piezoelectric, and electronic properties of the Janus BiXY (X = S, Se, Te and Y = F, Cl, Br, I) monolayers

M. Jahangirzadeh Varjovi ⬤ and E. Durgun ⬤[*]

UNAM–National Nanotechnology Research Center and Institute of Materials Science and Nanotechnology, Bilkent University, Ankara 06800, Turkey

Broken inversion symmetry in atomic structure can lead to the emergence of specific functionalities at the nanoscale. Therefore, realizing 2D materials in Janus form is a growing field, which offers unique features and opportunities. In this paper, we investigate the structural, vibrational, elastic, piezoelectric, and electronic properties of Janus BiXY (X = S, Se, Te and Y = F, Cl, Br, I) monolayers based on first-principle methods. The structural optimization and vibrational frequency analysis reveal that all of the proposed structures are dynamically stable. Additionally, *ab initio* molecular dynamics simulations verify the thermal stability of these structures even at elevated temperatures. The mechanical response of the Janus BiXY crystals in the elastic regime is investigated in terms of in-plane stiffness and the Poisson ratio, and the obtained results ascertain their mechanical flexibility. The piezoelectric stress and strain coefficient analysis demonstrates the appearance of strong out-of-plane piezoelectricity, which is comparable with the Janus transition metal dichalcogenide monolayers. The calculated electronic band structures reveal that except for BiTeF, all Janus BiXY monolayers are indirect band gap semiconductors, and their energy band gaps span from the infrared to the visible part of the optical spectrum. Subsequently, large Rashba spin splitting is observed in electronic band structures when the spin-orbit coupling is included. The obtained results point out Janus 2D BiXY structures as promising materials for a wide range of applications in nanoscale piezoelectric and spintronics fields.

DOI: 10.1103/PhysRevMaterials.5.104001

I. INTRODUCTION

Two-dimensional (2D) ternary metal chalcogenides (i.e., MXY) [1–8] are emerging as next-generation 2D semiconductors beyond their binary counterparts [9,10]. Especially, bismuth-based ternary compounds, such as bismuth oxychalcogenides (Bi$_2$O$_2X$ with X = S, Se, and Te), have been realized and have attracted considerable interest due to their remarkable properties, including high carrier mobility and stability at ambient conditions [11,12]. Furthermore, recent experimental studies show that bismuth oxyhalides (BiOX with X = Cl, Br, and I) have excellent photocatalytic performance owing to their unique electronic properties [13]. Another important family of bismuth-based ternary structures is bismuth tellurohalides (BiTeX with X = Cl, Br, and I), which have been shown to possess a strong Rashba spin splitting (RSS) [14,15].

Recently, single-layer (SL) BiTeI composed of three sublayers, with Bi atoms sandwiched between Te and I plates, has been isolated by exfoliation from bulk form [16]. Following this achievement, fascinating properties of BiTeI, including giant RSS [17–19], large out-of-plane piezoelectricity [20,21], and high thermoelectric performance (ZT) [22,23], have been investigated extensively. In addition to BiTeI, various bulk bismuth chalcohalide structures (BiXY with X = S, Se, Te and Y = Cl, Br, I) composed of weakly coupled layers have been synthesized. For instance, bulk

BiTeBr [24], BiTeCl [25], BiSeI [26], and BiSI [27,28] have been realized in their multilayered form, and their fundamental physical properties have been studied, both theoretically and experimentally [29–32]. In this regard, thermoelectric properties of bulk- and SL-BiTeBr have been investigated by using first-principles calculations, and enhanced thermoelectric performance of SL-BiTeBr compared to the bulk structure (owing to reduced thermal conductivity) has been revealed [33]. In another experimental study, it has been reported that the BiTeCl is a semiconductor with an electronic band gap of 0.77 eV at room temperature, which makes it a suitable material for infrared detector and sensing applications [34,35]. The vibrational properties of bulk and exfoliated flakes of BiTeCl have been examined by Raman spectroscopy, providing basic information on lattice dynamics [36]. Furthermore, theoretical calculations and experimental analysis have demonstrated pressure-induced topological phase transitions and superconductivity in BiTeX crystals [37–39]. Additionally, bulk crystals of BiSI and BiSeI, which are stable at high temperatures, have been synthesized in large quantities by a ball milling method and have been shown to exhibit suitable optical band gaps for solar cell applications [40]. Lately, highly crystalline 2D BiTeCl and BiTeBr nanosheets, which can be utilized in spintronics [41], have been directly synthesized via epitaxial growth [42].

Despite promising outcomes of experimental and theoretical research on bismuth chalcohalides, a comprehensive and comparative study focusing on the design and characterization of BiXY monolayers has not been performed. With this

─────────
[*]durgun@unam.bilkent.edu.tr

motivation, we systematically investigated the structural, vibrational, mechanical, piezoelectric, and electronic properties of the Janus BiXY ($X =$ S, Se, Te and $Y =$ F, Cl, Br, I) monolayers using first-principles techniques. First, the ground state configurations of the BiXY monolayers are obtained, and the corresponding structural parameters and cohesive energies are reported. Next, the dynamical and thermal stability of the systems is tested by phonon spectrum analysis and *ab initio* molecular dynamic (AIMD) simulations. The structural stability, vibrational properties, and Raman spectrum of each structure are investigated. Next, the mechanical response in the elastic regime and piezoelectric response is examined. Finally, the electronic properties are studied, and the effect of spin-orbit coupling (SOC) on electronic band structures, including Rashba splitting, is analyzed.

II. METHODOLOGY

In this study, we utilized the Vienna *Ab initio* Simulation Package (VASP) [43–46] to perform first-principles calculations based on density functional theory (DFT) [47,48] with projector-augmented wave (PAW) [49] potentials. For the exchange-correlation interaction, the Perdew-Burke-Ernzerhof (PBE) functional within the generalized gradient approximation (GGA) was considered [50]. A plane-wave basis set with the kinetic cutoff energy of 520 eV was employed for all calculations. The Brillouin zone (BZ) was sampled uniformly by a Γ-centered $16 \times 16 \times 1$ k-point mesh based on the Monkhorst-Pack scheme [51]. The total energy convergence criterion for relaxation between the sequential steps was set to 10^{-5} eV. The ionic positions and lattice constants of the structures were optimized until the Hellmann-Feynman forces on each atom were decreased below 0.01 eV/Å, while the pressure on the lattice was reduced below 1.0 kbar. To hinder the artificial interactions in the nonperiodic direction, a vacuum space of ~15 Å was inserted. During the calculation of electronic band structures, the spin-orbit coupling (SOC) effect was also taken into account [52]. Additionally, the hybrid functional of Heyd-Scuseria-Ernzerhof (HSE06) was adopted with SOC to obtain corrected band gaps [53,54]. The HSE06 functional was designed by mixing 25% of nonlocal Fock exchange with 75% of PBE exchange and 100% of PBE correlation energy. The phonon dispersions were calculated for $4 \times 4 \times 1$ supercells by using a small-displacement method as implemented in PHONOPY [55]. To check the thermal stability of the proposed structures, *ab initio* molecular dynamics (AIMD) calculations were carried out via implementing a micro-canonical ensemble method for a total simulation time of 2 ps with 1 fs time step. The vibrational modes and atomic displacements were obtained by a direct diagonalization of the force constant matrix. The corresponding first-order off-resonant Raman spectrum of each vibrational mode was determined via calculating the macroscopic dielectric tensor at the Γ point of the BZ by using a small-difference method [56]. Due to the net electric dipole moment occurring in the polar surface calculations, the dipole correction was taken into account [57]. Both elastic constants and piezoelectric stress coefficients were calculated by employing the density functional perturbation theory (DFPT) method with a $48 \times 48 \times 1$ k-point grid and cutoff energy of 700 eV.
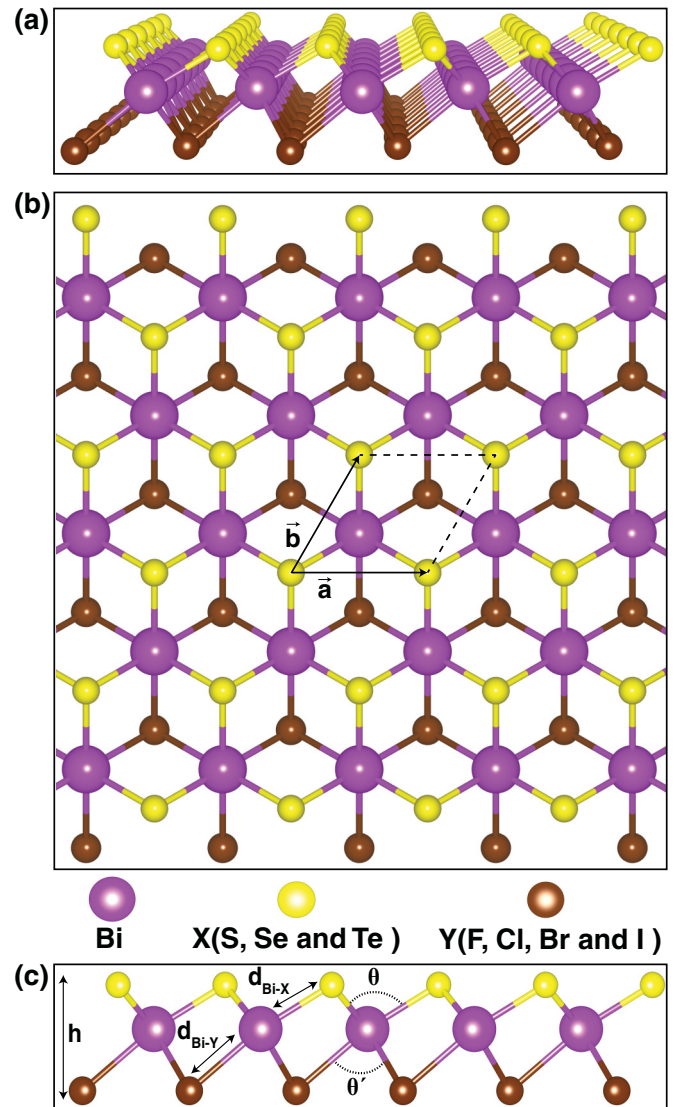

FIG. 1. (a) Perspective, (b) top, and (c) side views of Janus BiXY monolayers. The corresponding lattice vectors (a, b), bond lengths ($d_{\text{Bi-}X}$, $d_{\text{Bi-}Y}$), bond angles between X-Bi-X and Y-Bi-Y (θ and θ'), and thickness (h) are shown.

To analyze the net charge on atoms and the bond characteristics of the structures, the Bader technique was applied [58].

III. RESULTS AND DISCUSSION

A. Atomic structure and energetics

The geometric structure of the Janus BiXY ($X =$ S, Se, Te and $Y =$ F, Cl, Br, I) monolayers is constructed based on the crystal structure of the realized BiTeI monolayer. The schematic representation of the Janus BiXY monolayers is depicted in Fig. 1. The primitive cell of SL-BiXY consists of three atomic sublayers where Bi is in the center while X and Y atoms are located on the top and bottom layers, respectively. Their symmetry belongs to the $P3m1$ space group and C_{3v} point group. Additionally, similarly to several Janus transition metal dichalcogenide (TMD) monolayers [59,60], their structure lacks the reflection symmetry with respect to

TABLE I. The optimized lattice constant (a), atomic bond lengths ($d_{\text{Bi-}X}$, and $d_{\text{Bi-}Y}$), thickness (h), bond angles between X-Bi-X and Y-Bi-Y (θ and θ'), cohesive energy per atom (E_C), the amounts of charge transfer, $\Delta\rho_{(\text{Bi-}X)}$ and $\Delta\rho_{(\text{Bi-}Y)}$, the calculated work functions for two different surfaces, Φ_X and Φ_Y, and their differences, $\Delta\Phi$.

Structure	a (Å)	$d_{\text{Bi-}X}$ (Å)	$d_{\text{Bi-}Y}$ (Å)	h (Å)	θ (deg)	θ' (deg)	E_C (eV/atom)	$\Delta\rho_{(\text{Bi-}X)}$ (e^-)	$\Delta\rho_{(\text{Bi-}Y)}$ (e^-)	Φ_X (eV)	Φ_Y (eV)	$\Delta\Phi$ (eV)
BiSF	3.94	2.73	2.50	2.55	92.4	103.7	3.58	0.74	0.76	6.09	5.52	0.57
BiSCl	4.06	2.75	2.93	3.18	95.4	87.7	3.06	0.75	0.58	5.85	6.13	−0.28
BiSBr	4.11	2.75	3.07	3.35	96.4	83.9	2.90	0.75	0.51	5.69	5.70	−0.01
BiSI	4.19	2.76	3.25	3.51	98.6	80.1	2.75	0.76	0.40	5.70	5.28	0.42
BiSeF	4.01	2.84	2.52	2.64	89.7	105.5	3.42	0.60	0.76	5.77	5.52	0.25
BiSeCl	4.15	2.86	2.94	3.28	92.6	89.7	2.92	0.61	0.59	5.49	6.07	−0.58
BiSeBr	4.19	2.87	3.07	3.45	93.5	85.7	2.77	0.61	0.51	5.41	5.74	−0.33
BiSeI	4.27	2.88	3.27	3.64	95.5	81.6	2.61	0.62	0.41	5.30	5.20	0.10
BiTeF	4.15	3.02	2.55	2.74	86.8	108.2	3.24	0.40	0.77	4.74	4.92	−0.18
BiTeCl	4.31	3.06	2.96	3.38	89.7	93.3	2.77	0.42	0.59	5.08	6.05	−0.97
BiTeBr	4.35	3.06	3.09	3.56	90.4	89.2	2.62	0.42	0.52	4.98	5.74	−0.76
BiTeI	4.42	3.07	3.28	3.78	92.1	84.6	2.46	0.42	0.41	4.84	5.24	−0.40

the center atom. The calculated structural parameters of BiXY monolayers are listed in Table I. The obtained results are in good agreement with the available data on BiTeCl, BiTeBr, and BiTeI [20,21,61,62]. Additionally, our calculated lattice constant (4.42 Å) is comparable to the in-plane lattice constant of synthesized bulk BiTeI (4.33 Å) [63]. The bond length between Bi and X/Y atoms ($d_{\text{Bi-}X}$ and $d_{\text{Bi-}Y}$) elongates going down in the chalcogen and/or halogen group. This is due to the increase in the atomic radius of X and/or Y atoms in the structures. Accordingly, BiTeI and BiSF monolayers possess the longest and shortest bond lengths, respectively. The lattice constant (a) follows a similar trend with the bond length, and for each subset of X, a enlarges down the halogen group and vice versa. The thickness of the Janus BiXY crystals (h) increases with elongation of $d_{\text{Bi-}X}$ and $d_{\text{Bi-}Y}$ as it is proportional with the bond length. On the other hand, for a given X, the bond angle θ' ($\angle Y$-Bi-Y) narrows down the halogen group, whereas θ ($\angle X$-Bi-X) represents an opposite behavior. This is due to the fact that when the electronegativity difference between X and Y atoms ($\Delta\chi$) increases, more electrons accumulate around the atom with higher electronegativity; in turn, the atoms start to repel each other, which results in widening of the bond angle.

The cohesive energy per atom (E_C) for the proposed structures is calculated via the following relation:

$$E_C = \frac{[E_T(\text{Bi}) + E_T(X) + E_T(Y)] - [E_T(\text{Bi}XY)]}{3}, \quad (1)$$

where $E_T(\text{Bi})$, $E_T(X)$, and $E_T(Y)$ are the single-atom energies of Bi, X, and Y elements, respectively; $E_T(\text{Bi}XY)$ corresponds to the total energy of the Janus BiXY structures. All obtained results are given in Table I. Correlated with the bond weakening, E_C gradually decreases as a enlarges. In a similar manner, for each subset of X (Y), E_C decreases moving down the chalcogen (halogen) group. High cohesive energy implies strong binding between the constituent elements and is a notable parameter to quantify the stability of a material. Accordingly, BiSF and BiTeI are the most and the least stable structures among Janus BiXY monolayers. It should be noted that the computed E_C's are comparable to the other

bismuth-based systems. For instance, E_C of 2D Bi_2Se_3, Bi_2Te_2S, and Bi_2Te_2Se is reported to be 2.89, 2.77, and 2.67 eV/atom [64], respectively, which is within the same cohesive energy range of the BiXY monolayers.

In BiXY systems, the size difference of atoms, electronegativity difference ($\Delta\chi$), and different types of bonding between Bi-X and Bi-Y (double and single bonding, respectively) give rise to inequivalent charge distributions. The corresponding data from Bader analysis demonstrate that the charge depletion from Bi to X and Y elements ($\Delta\rho_{(\text{Bi-}X)}$ and $\Delta\rho_{(\text{Bi-}Y)}$) decreases with increasing a, which is correlated with the aforementioned factors and also supports the variation of E_C. The general features of charge partitioning between the atoms reveal that the Bi layer in all structures is positively charged, whereas the X and Y layers are negatively charged. As an example, the results of Bader analyses show that 0.42 e^- and 0.41 e^- are transferred from Bi to Te and I atoms, respectively, which is consistent with previous studies on BiTeI crystals [20]. The unbalance charge between the X and Y sides generates a net electric field between Bi layer and $X(Y)$ layer, the direction of which points Bi layer to the $X(Y)$ layer. Furthermore, the charge difference between the surfaces affects the magnitude of the thermionic work function (Φ) on each side. Accordingly, to identify the inherent electric field in Janus BiXY crystals, the work function from X and Y sides are calculated. The planar average of the electrostatic potential and the related work functions for Bi-X and Bi-Y surfaces (Φ_X and Φ_Y) are displayed in Fig. 2. It is noticed that the difference between Φ_X and Φ_Y ($\Delta\Phi$) is proportional with magnitude of the dipole moment in the structures and is in parallel with the Helmholtz equation [65], $\mu = \frac{e}{\varepsilon_0} \times \frac{\Delta\Phi A}{\theta}$. Based on the Helmholtz model, the surface dipole (μ) is linearly proportional with the work function difference ($\Delta\Phi$), slab surface area (A), and elementary charge (e), and has inverse relation with the surface coverage (θ) and vacuum permittivity (ε_0) [65]. In addition, the electrostatic potential difference between X and Y surfaces increases when $\Delta\chi$ is larger. For the BiXF monolayers, the potential energy on the side of F is minimal, which is due to the fact that the strong electronegativity of F atoms that causes the accumulated electrons cannot offset it.
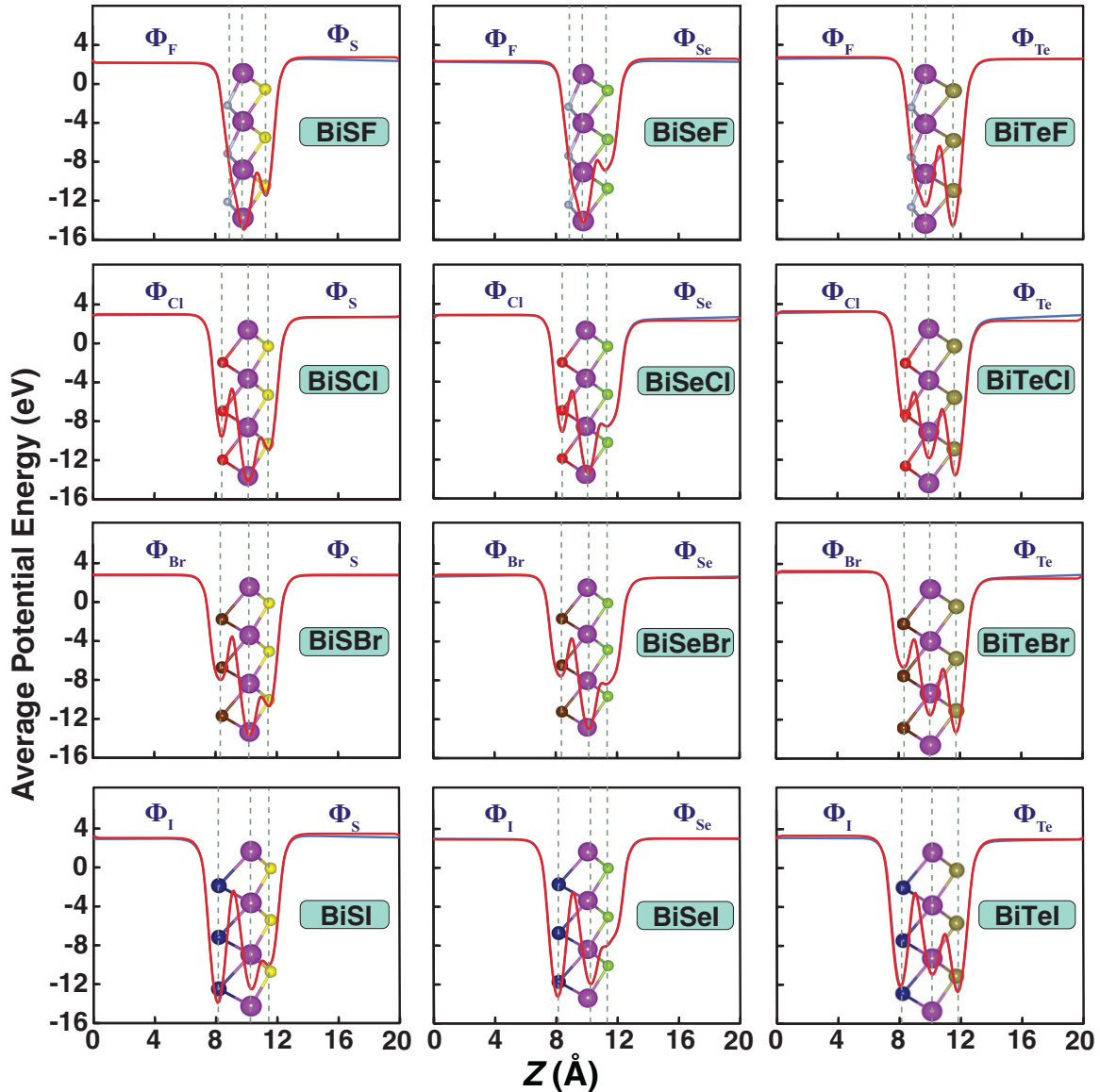
FIG. 2. Planar average of the electrostatic potential along the z axis for Janus BiXY monolayers with (red) and without (blue) dipole correction. The vertical dashed lines represent the positions of the Bi, X, and Y atoms. Φ_X and Φ_Y denote the work function of the X and Y surfaces, respectively.

The electrostatic potential energy diagram demonstrates information about the charge distribution between the constituent elements in the structures. Generally, a high electrostatic potential implies the deficiency of electrons on that element, whereas the low electrostatic potential indicates an abundance of electrons. Since the F atom has the highest electronegativity value, it attracts the majority of the electrons, decreasing the electrostatic potential energy. Moreover, the change in the work function of the BiTeBr monolayer is almost twice as large as the one for BiTeI, which results in a larger dipole moment in the BiTeBr, as was also previously verified by earlier work [17].

B. Dynamical stability

The structural stability of Janus BiXY monolayers is examined by phonon spectra analyses, and Fig. 3 shows that the

dispersion of the phonon modes is free from any imaginary frequencies, and all twelve structures are confirmed to be stable. The primitive cell of the SL-BiXY crystals consists of three atoms, resulting in 9 vibrational modes. The three acoustic phonon modes are the flexural acoustic (ZA) branch, the transverse acoustic (TA) branch, and the longitudinal acoustic (LA) branch. The ZA phonon mode has quadratic dispersion while TA and LA phonon modes have linear dispersion near the Γ point, as in other 2D systems anticipated by continuum elasticity theory [66]. It can be seen from Fig. 3 that when the atomic mass of the elements becomes heavier for a given structure, all phonon modes are pushed toward lower frequencies, and overall phonon spectra are narrowed. Additionally, in BiXF and BiTeY monolayers, a gap is noticed between acoustical and optical frequencies, which is due to the large mass differences between the constituent elements and weakened bond strength between the atoms. For the remaining
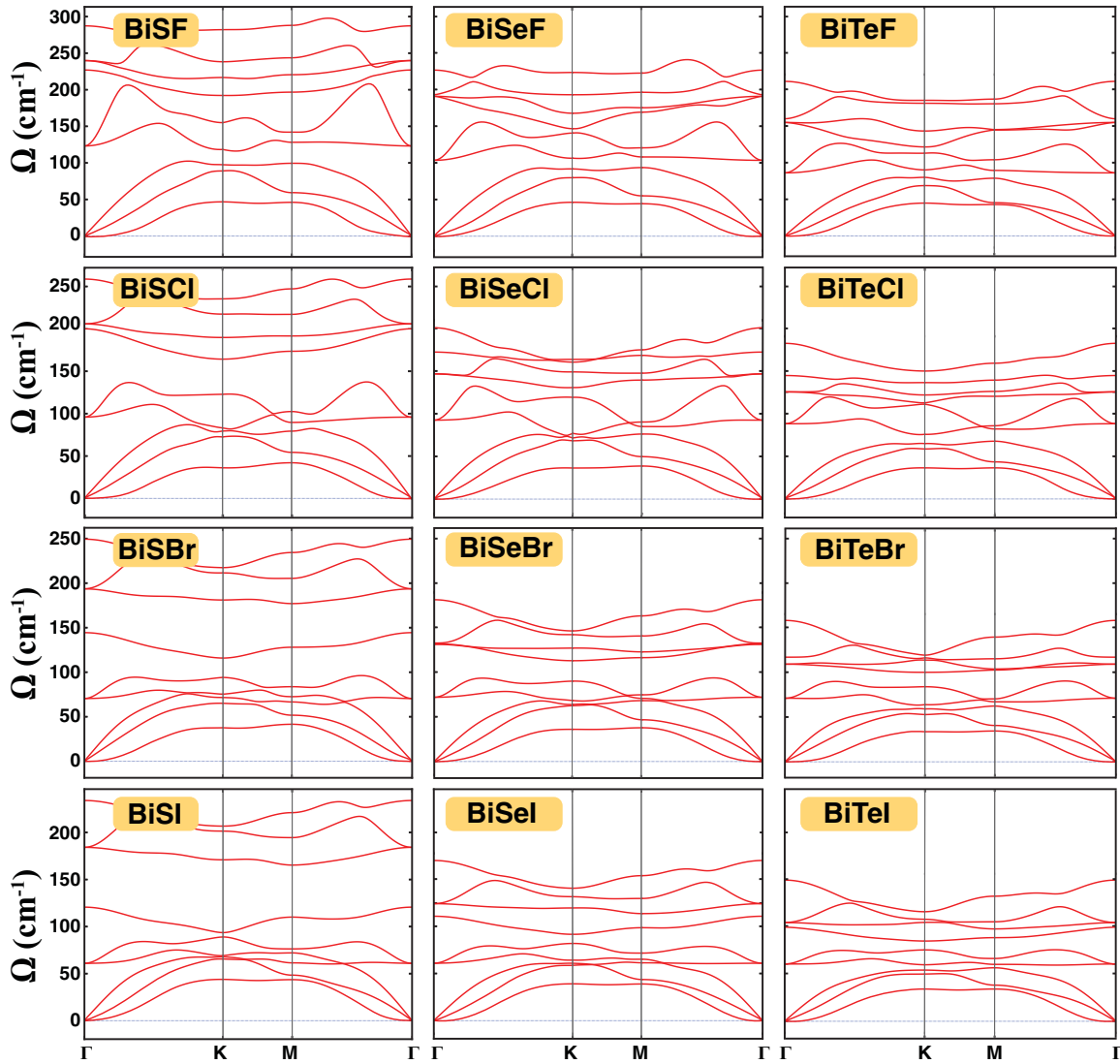
FIG. 3. Phonon band diagrams of the Janus BiXY monolayers.

structures, the low-frequency optical and acoustic branches overlap. The phonon band gap reduces the phonon-phonon scattering rate (i.e., long phonon relaxation time) and leads to enhanced thermal conductivity [67–69].

To test the stability of the structures at high temperatures, *ab initio* molecular dynamics (AIMD) simulations were carried out at 300 K and 600 K for 2 ps. To alter the unit cell size constraint, a $4 \times 4 \times 1$ supercell was used for BiXY monolayers. The variation of energy as a function of simulation time and the final snapshots of the resulting structures at 300 K and 600 K are illustrated in Fig. 4, and Fig. S1, Supplemental Material [70]. AIMD simulations indicate that apart from slight distortions, which are not sufficient enough to break the Bi-X and Bi-Y bonds, the crystalline forms of BiXY monolayers are preserved even at elevated temperatures and confirm the thermal stability.

C. Vibrational properties

Vibrational properties and the corresponding Raman spectra are closely related to the geometrical structure of the

materials, and their analysis could be a useful technique to investigate the physical properties related to the lattice symmetries. Due to the C_{3v} symmetry, the six optical vibration modes are either nondegenerate or doubly degenerate at the Γ point. The irreducible representation of the corresponding optical phonons in the center of the BZ (Γ point) for the Janus BiXY monolayers is given by $\Gamma^{C_{3v}} = 2A_1 + 2E$, where the E modes are assigned to the doubly degenerate in-plane displacements, whereas the nondegenerate A_1 modes are attributed to the vibration of the atoms along the z direction. Both A_1 and E eigenmodes are Raman- and IR-active modes since in the structures with C_{3v} symmetry, A_1 and E modes correspond to the linear and quadratic functions in the character table. Thus, the vibrational mode analysis of Janus BiXY monolayers reveals 4 peaks corresponding to the Raman- and IR-active modes. In a Raman experiment, the material is exposed to the light beams, and the scattered photons are immediately collected. The dispersion of the collected photons determines the Raman spectrum of the sample with respect to the frequency shift. According to the Raman theory, inelastically scattered photons originating from the oscillation
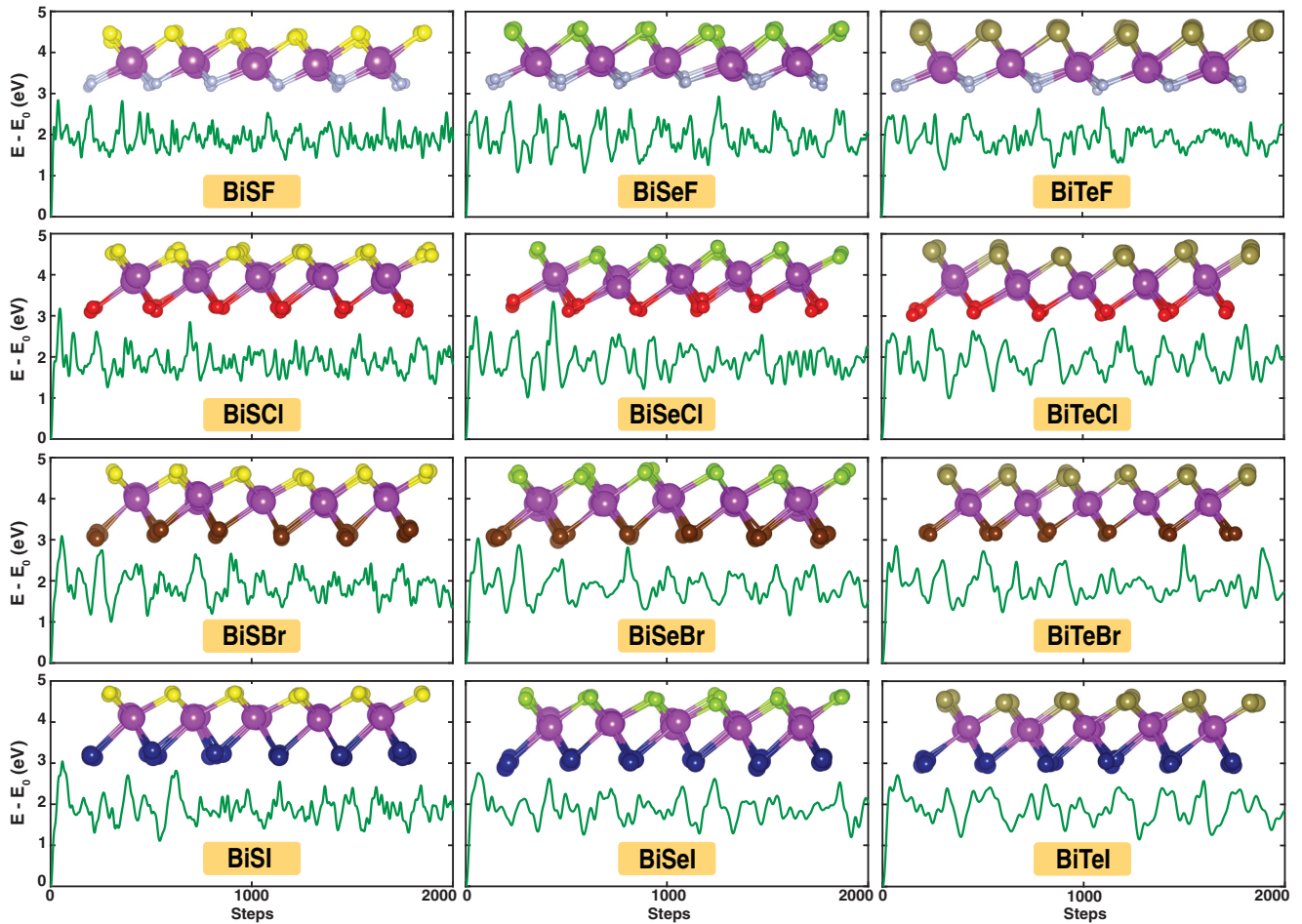
FIG. 4. The variation of energy with respect to the number of steps at 300 K for Janus BiXY crystals. The insets show the snapshots of atomic configurations at the end of *ab initio* molecular dynamics (AIMD) simulations for each structure.

of dipole moments of the crystal correspond to the Raman-active vibrational modes. The Raman intensity of a structure is mainly affected by incident light source wavelength and intensity, the concentration of the sample, and the scattering properties of the material [71]. The calculated Raman spectra of Janus BiXY crystals are illustrated in Figs. 5(a)–5(c). The atomic displacements of the Raman-active modes are labeled on each spectrum to identify the origins of the Raman peaks. Depending on the atomic mass and bond strength, the Raman activities of the structures differ from each other. By going from the lightest (BiSF) to the heaviest (BiTeI) monolayer in the proposed systems, the Raman spectra shift toward lower frequencies mainly attributed to the increased mass and bond strength. In addition, for each subset of Y, the intensity of the $E^{(\text{Bi-}Y)}$ Raman peak increases down the chalcogen group. Our results point out that the most prominent Raman-active mode in BiXF is $A_1^{(\text{Bi-}X)}$ while for BiTeY ($Y=$ Br and I) structures, the $E^{(\text{Bi-Te})}$ mode is the most significant peak in the spectrum. For BiTeBr and BiTeI, the theoretical Raman spectra can be compared with the experimental data. Sklyadneva *et al.* demonstrated that the synthesized BiTeBr and BiTeI crystals possess four Raman-active modes, the most prominent of which appear at the frequencies of 98.5 and 99 cm^{-1}, respectively [72]. The highest calculated Raman-active mode frequency is 108 cm^{-1} for BiTeBr and 103 cm^{-1} for BiTeI

monolayers. The comparisons reveal that our results are in agreement with the experimental findings on synthesized bismuth tellurohalides. The intensity of the peaks in the spectrum is due to the contribution of macroscopic dielectric constants of vibrational modes to the Raman tensors. For BiSeF and BiTeF monolayers, the $E^{(\text{Bi-F})}$ Raman mode, and for BiTeI, the $A_1^{(\text{Bi-I})}$ mode, vanishes, which indicates that their intensity is too weak to observe. To better explain the vibrational character of the BiXY monolayers, the BiSeI monolayer is considered as a prototype to exemplify the four distinct atomic displacements in the optical spectrum, and the corresponding results are illustrated in Fig. S2, Supplemental Material [70].

D. Mechanical and piezoelectric properties

After revealing the structural stability, the elastic strain tensor is computed to study the mechanical properties of the proposed structures, and the nonzero elastic constants (C_{ij}) are listed in Table II. First, it should be noted that all Janus BiXY monolayers satisfy the Born and Huang criteria [73,74] [$C_{11} > |C_{12}|$ and $C_{66} = (C_{11} - C_{12})/2 > 0$ for hexagonal lattice], indicating the mechanical stability. The elastic properties of the BiXY monolayers are examined in terms of two constants: the in-plane stiffness (Y_{2D}) and the Poisson ratio (ν). The Y_{2D}, which is the 2D analog to Young's modulus
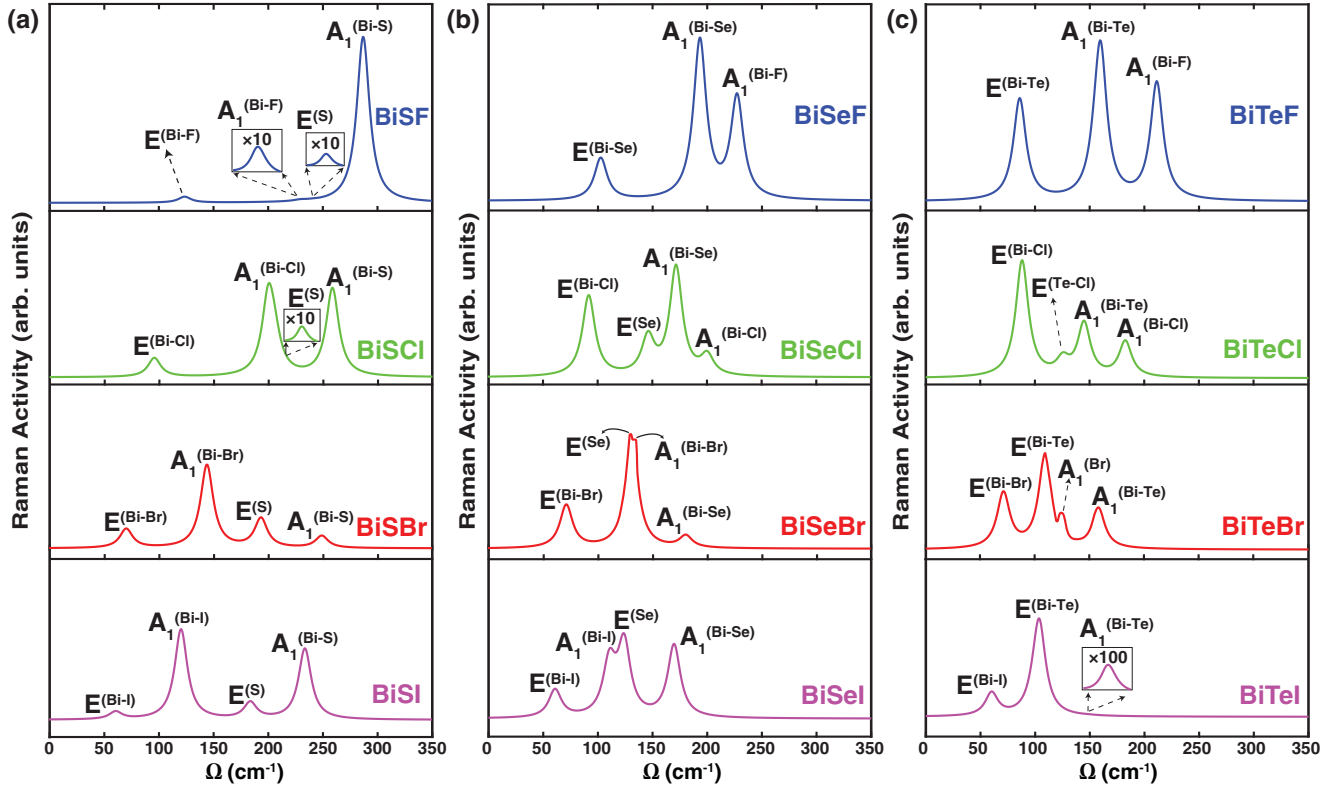
FIG. 5. The normalized Raman activity spectra for (a) BiSY, (b) BiSeY, and (c) BiTeY monolayers.

in 3D structures, is a measure of stiffness or flexibility of the materials. For the BiXY monolayers, the Y_{2D} is obtained by using the following relation, $Y_{2D} = (C_{11}^2 - C_{12}^2)/C_{11}$, and the results are summarized in Table II. For each subset of X (Y), Y_{2D} decreases down the chalcogen (halogen) group, which is related with the elongation of the bonds (d_{Bi-X} and d_{Bi-Y}), i.e., weakening of the bonds between the atoms. Accordingly, the highest and lowest Y_{2D} is obtained for BiSF and BiTeI, respectively. A similar trend is also noticed in binary and ternary TMDs [75]. The Y_{2D} values are between 25–42 N/m, indicating that BiXY monolayers are not stiff. While the obtained values are smaller than Y_{2D} of Janus TMDs, such as MoXY

and WXY, they are within the same range of CrXY and VXY [75,76]. Next, the Poisson ratio ($\nu = C_{12}/C_{11}$), which is the ratio of the transverse contraction strain to the axial extension strain in the direction of the stretching force, is computed (Table II). The calculated ν values are less than 1/3 (except BiSI), which implies that Janus BiXY monolayers are brittle based on the Frantsevich rule [77]. Additionally, in terms of bonding character, $\nu \approx 0.25$ marks a transition from ionicity to metallicity [78]; therefore, for all the structures, the bonding nature is mainly ionic with a small metallic contribution.

Piezoelectricity is described as a coupling between electrical polarization and mechanical stress and can be produced

TABLE II. For the BiXY Janus monolayers, relaxed-ion elastic coefficients, C_{ij}, in-plane stiffness, Y_{2D}, and Poisson ratio, ν, piezoelectric stress coefficients, e_{ij}, and the corresponding piezoelectric strain coefficients, d_{ij}. Note that the values of e_{ij} are multiplied by 10^{-10}.

| Structure	$C_{11} = C_{22}$ (N/m)	C_{12} (N/m)	Y_{2D} (N/m)	ν (−)	e_{11} (C/m)	e_{31} (C/m)	d_{11} (pm/V)	d_{31} (pm/V)
BiSF	45	12	42	0.26	3.06	−0.19	9.11	−0.33
BiSCl	35	10	32	0.29	4.12	−0.13	16.61	−0.29
BiSBr	34	11	31	0.32	4.41	−0.18	19.11	−0.41
BiSI	33	11	29	0.34	5.09	−0.24	23.11	−0.54
BiSeF	43	11	40	0.26	1.22	−0.11	3.81	−0.20
BiSeCl	33	9	30	0.27	2.68	−0.11	11.20	−0.26
BiSeBr	32	9	29	0.29	3.03	−0.16	13.51	−0.40
BiSeI	31	10	28	0.31	3.65	−0.23	17.12	−0.57
BiTeF	39	11	36	0.27	−2.45	0.04	−8.54	0.07
BiTeCl	30	7	28	0.24	0.75	−0.07	3.29	−0.18
BiTeBr	28	7	26	0.26	1.21	−0.11	5.78	−0.31
BiTeI	27	7	25	0.27	1.87	−0.19	9.53	−0.56
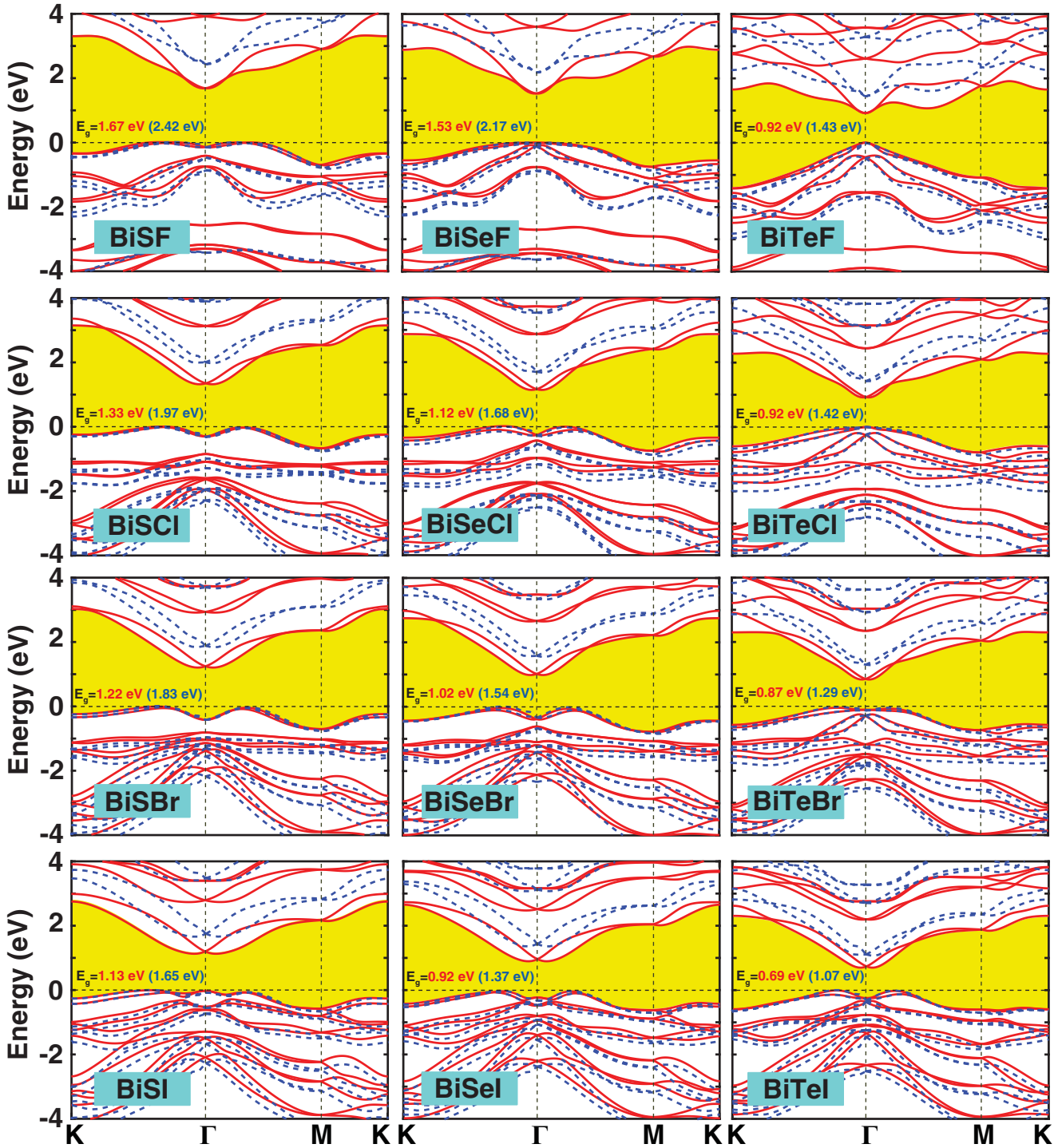
FIG. 6. Calculated electronic band structures for Janus BiXY monolayers by using GGA-PBE + SOC and HSE06 + SOC are shown by red solid and dashed blue lines, respectively. The fundamental band gaps are shaded yellow. The Fermi level is set to zero.

when applied external stress generates electric dipole moments in the noncentrosymmetric materials (and vice versa) [79]. For 2D materials, the piezoelectric stress coefficients, e_{ij}, must be renormalized by the z-axis lattice parameter [80], i.e., $e_{ij}^{2D} = z \times e_{ij}^{3D}$. Recent experimental observations and theoretical studies have shown an enhancement of piezoelectric constants in 2D materials compared to their 3D counterparts [81,82]. The relaxed-ion piezoelectric tensor, e_{ij}, in 2D

materials can be defined as sum of ionic e_{ij}^{ion} and electronic contributions e_{ij}^{el},

$$e_{ij} = e_{ij}^{el} + e_{ij}^{ion};$$ (2)

the e_{ij}'s are calculated by the DFPT method, and the values of piezoelectric strains, d_{ij}, are derived by using the relation

$$e_{ij} = d_{ik}C_{kj},$$ (3)

where C_{ij} is the elastic tensor of the related materials. The crystal symmetry of the structures determines the number of independent components in the piezoelectric tensors (e_{ij} and d_{ij}). Due to the C_{3v} symmetry of the Janus BiXY monolayers, the piezoelectric tensor in these structures has two independent coefficients, i.e., e_{11}/d_{11} for in-plane piezoelectricity and e_{31}/d_{31} for out-of-plane piezoelectricity. The out-of-plane piezoelectric constants of the 2D materials are affected by out-of-plane asymmetry and charge density difference on two surfaces. The Voigt notation of Janus BiXY monolayers can be defined as

$$e = \begin{pmatrix} e_{11} & -e_{11} & 0 \\ 0 & 0 & -e_{11} \\ e_{31} & e_{31} & 0 \end{pmatrix}, \quad d = \begin{pmatrix} d_{11} & -d_{11} & 0 \\ 0 & 0 & -2d_{11} \\ d_{31} & d_{31} & 0 \end{pmatrix}.$$

The relations between the piezoelectric tensor coefficients for Janus BiXY monolayers are given by [1,81,83]

$$d_{11} = \frac{e_{11}}{c_{11} - c_{12}}, \quad d_{31} = \frac{e_{31}}{c_{11} + c_{12}}. \quad (4)$$

The computed piezoelectric coefficients are summarized in Table II. As can be seen, e_{ij} increases down the halogen and/or chalcogen group. As a comparison, for single-layer MoS$_2$ and MoSSe structures, the e_{11} is reported to be 3.7×10^{-10} and 3.8×10^{-10} C/m, respectively [84]. The calculated values for BiSY and BiSeY monolayers are in the range of (1.22–5.09×10^{-10} C/m), while for BiTeY structures, the e_{11} component is found to be smaller than most of the TMX_2 and Janus TMXY crystals. However, the obtained results of d_{11} for BiTeY monolayers are much larger than the predicted values for the TMX_2 and Janus TMXY crystals [81,83]. The calculated piezoelectric coefficients, e_{11} (d_{11}), of the SbTeI monolayer are reported as 2.69×10^{-10} C/m (12.95 pm/V), which are slightly larger than their Janus bismuth counterparts [21]. In the case of 1T-TMDs, the piezoelectric coefficients are expected to be very small due to the central symmetry of the structures [59], while for BiXY crystal structures because of lack of inversion and mirror symmetry with respect to the Bi atoms, both in-plane and out-of-plane piezoelectric constants are significant. For ultrathin materials, large values of out-of-plane piezoelectricity are desired for applications in electromechanical devices. The d_{31} coefficients are calculated to be -0.54, -0.57, and -0.56 pm/V for BiSI, BiSeI, and BiTeI, respectively, which are larger than that of 2D Janus TMD structures such as MoSSe (0.29 pm/V) [1], MoSTe (0.4 pm/V) [83], and 1H-WSO (0.4 pm/V) [85]. Such a large out-of-plane piezoelectricity makes Janus BiXI monolayers suitable candidates for applications in piezoelectric devices.

E. Electronic properties

Lastly, the electronic properties of the Janus BiXY monolayers are analyzed. The electronic band structures are calculated initially at the level of GGA-PBE. As shown in Fig. 6, all structures are semiconductors, and except for BiTeF, they have indirect band gaps. Due to the presence of heavy elements such as Bi, Te, and I and the broken inversion symmetry of the structures, the inclusion of the spin-orbit coupling (SOC) effect is necessary. The inclusion of SOC reduces the band gap ($E_g^{\text{PBE-SOC}}$), and the effect is more dramatic as the
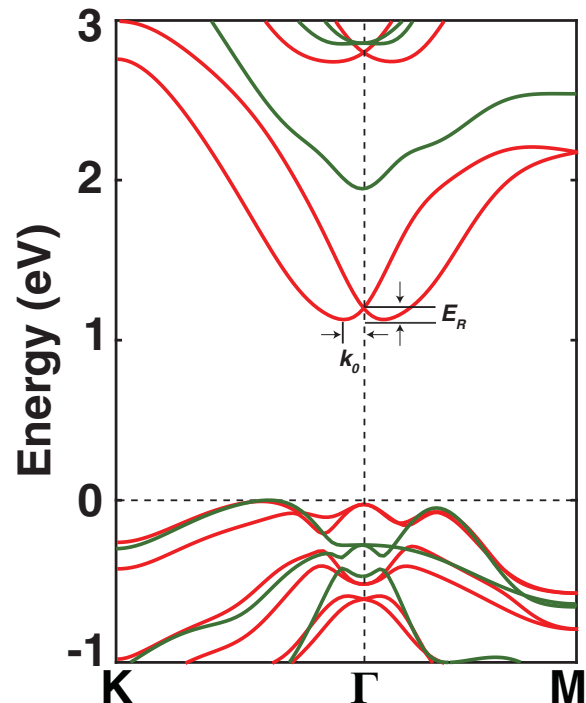

FIG. 7. Close-up view of the electronic band structure of BiSI monolayer around the Γ point and along the K-Γ-M points to exhibit the momentum offset k_o and the Rashba energy E_R. PBE and PBE-SOC results are shown by dark green and red lines, respectively.

elements get heavier. When the calculations are repeated with the HSE + SOC method, similar band profiles but widened band gaps ($E_g^{\text{HSE-SOC}}$) are obtained (Fig. 6). For a given subset, $E_g^{\text{HSE-SOC}}$ decreases moving down the chalcogen and halogen group, which is correlated with the charge transfer ($\Delta\rho_{(\text{Bi-}X)}$ and $\Delta\rho_{(\text{Bi-}Y)}$). $E_g^{\text{HSE-SOC}}$ is between 1.07 eV to 2.42 eV and covers a range from infrared to visible parts of the optical spectrum. The calculated partial density of states (PDOS) of the Janus BiXY monolayers is shown in Fig. S3, Supplemental Material [70]. It is seen that for the structures with the same halogen atom, the PDOS diagrams are similar to each other. Our results indicate that the states near the valence band maximum (VBM) are mainly composed of X-p and Y-p orbitals. In contrast, the conduction band minimum (CBM) states are dominated by the Bi-p orbital in all structures which is in good agreement with the previous studies on BiTeX crystals [61,62]. It is noticed that the spin-orbit splitting in energy bands is more significant in the structures with heavier elements and more distinct broken inversion symmetry. Since the electronic band structure profiles of Janus BiXY monolayers are similar to each other, BiSI is chosen as a prototype to represent the band splitting near the Γ point. As seen from Fig. 7, the degenerate conduction band minimum (CBM) is reduced to the lower energies and split into two branches following the inclusion of SOC. This can be considered as valid evidence of the Rashba splitting in the system. The strength of the Rashba splitting can be defined by two parameters: momentum offset (k_o) and the Rashba energy (E_R). The relation between these two terms and the Rashba coefficient (α_R) is given by $\alpha_R = 2E_R/k_o$. The α_R of 2D materials should

TABLE III. Energy band gaps at the level of GGA-PBE, E_g^{PBE}; GGA-PBE + SOC, $E_g^{\text{PBE-SOC}}$; HSE06 + SOC, $E_g^{\text{HSE-SOC}}$; the Rashba energy, E_R; and the Rashba coefficient, α_R, for the BiXY Janus monolayers.

Structure	E_g^{PBE} (eV)	$E_g^{\text{PBE-SOC}}$ (eV)	$E_g^{\text{HSE-SOC}}$ (eV)	E_R (meV)	α_R (eVÅ)
BiSF	1.98	1.67	2.42	2	0.19
BiSCl	1.80	1.33	1.97	29	1.20
BiSBr	1.77	1.22	1.83	40	1.37
BiSI	1.93	1.13	1.65	71	1.67
BiSeF	2.01	1.53	2.17	2	0.20
BiSeCl	1.65	1.12	1.68	25	1.30
BiSeBr	1.56	1.02	1.54	34	1.44
BiSeI	1.63	0.92	1.37	64	1.98
BiTeF	1.69	0.92	1.43	0	0.00
BiTeCl	1.77	0.92	1.42	12	1.25
BiTeBr	1.60	0.87	1.29	17	1.27
BiTeI	1.52	0.69	1.07	40	1.80

be large enough to be used in spintronics applications. E_R and α_R for the Janus BiXY monolayers are computed and listed in Table III. It is noticed that, among the considered structures, BiXF (BiXI) monolayers have the lowest (highest) value of E_R and α_R. The obtained values of E_R and α_R for BiTeBr and BiTeI monolayers are in good agreement with the previous theoretical calculations [17,20].

IV. CONCLUSION

In summary, we have systematically investigated structural, vibrational, elastic, piezoelectric, and electronic properties of the Janus BiXY (X = S, Se, Te and Y = F, Cl, Br, I) monolayers. Our vibrational frequency analysis and *ab initio* molecular dynamics simulations up to 600 K reveal that all of the proposed Janus BiXY crystals are dynamically stable. The calculated Raman spectra exhibit that BiXY monolayers possess four typical Raman-active modes. To characterize the mechanical response in the elastic regime, the in-plane stiffness and Poisson ratio are calculated, and the results indicate that the considered systems are flexible and brittle. Following the calculation of the elastic tensors, the piezoelectric coefficients are computed, and large out-of-plane piezoelectric constants are obtained, especially for BiXI monolayers, which are greater than those of prominent TMDs. The electronic structure calculations show that except for BiTeF, which is a direct band gap semiconductor, the rest of the monolayers are indirect band gap semiconductors varying between 1.07 eV and 2.42 eV, which covers a range from the infrared to visible spectrum. The inclusion of spin-orbit coupling results in large band splitting and momentum shift in conduction band minimum near the Γ point, which indicates the Rashba effect in these systems. These intriguing properties suggest BiXY monolayers as suitable candidates for nanoscale piezoelectric and spintronics applications.

[1] L. Dong, J. Lou, and V. B. Shenoy, ACS Nano **11**, 8242 (2017).

[2] A.-Y. Lu, H. Zhu, J. Xiao, C.-P. Chuu, Y. Han, M.-H. Chiu, C.-C. Cheng, C.-W. Yang, K.-H. Wei, Y. Yang *et al.*, Nat. Nanotechnol. **12**, 744 (2017).

[3] R. Li, Y. Cheng, and W. Huang, Small **14**, 1802091 (2018).

[4] M. Demirtas, M. J. Varjovi, M. M. Cicek, and E. Durgun, Phys. Rev. Mater. **4**, 114003 (2020).

[5] L. Hu and D. Wei, J. Phys. Chem. C **122**, 27795 (2018).

[6] M. Yagmurcukardes, Y. Qin, S. Ozen, M. Sayyad, F. M. Peeters, S. Tongay, and H. Sahin, Appl. Phys. Rev. **7**, 011311 (2020).

[7] L. Zhang, Z. Yang, T. Gong, R. Pan, H. Wang, Z. Guo, H. Zhang, and X. Fu, J. Mater. Chem. A **8**, 8813 (2020).

[8] V. Van Thanh, N. D. Van, R. Saito, N. T. Hung *et al.*, Appl. Surf. Sci. **526**, 146730 (2020).

[9] A. Ramasubramaniam, Phys. Rev. B **86**, 115409 (2012).

[10] Q. Ji, Y. Zhang, Y. Zhang, and Z. Liu, Chem. Soc. Rev. **44**, 2587 (2015).

[11] M. Kang, H.-J. Chai, H. B. Jeong, C. Park, I.-y. Jung, E. Park, M. M. Çiçek, I. Lee, B.-S. Bae, E. Durgun *et al.*, ACS Nano **15**, 8715 (2021).

[12] J. Wu, C. Tan, Z. Tan, Y. Liu, J. Yin, W. Dang, M. Wang, and H. Peng, Nano Lett. **17**, 3021 (2017).

[13] J. Di, J. Xia, H. Li, S. Guo, and S. Dai, Nano Energy **41**, 172 (2017).

[14] K. Ishizaka, M. Bahramy, H. Murakawa, M. Sakano, T. Shimojima, T. Sonobe, K. Koizumi, S. Shin, H. Miyahara, A. Kimura *et al.*, Nat. Mater. **10**, 521 (2011).

[15] Y. Chen, M. Kanou, Z. Liu, H. Zhang, J. Sobota, D. Leuenberger, S. Mo, B. Zhou, S. Yang, P. Kirchmann *et al.*, Nat. Phys. **9**, 704 (2013).

[16] B. Fülöp, Z. Tajkov, J. Pető, P. Kun, J. Koltai, L. Oroszlány, E. Tóvári, H. Murakawa, Y. Tokura, S. Bordács *et al.*, 2d Mater. **5**, 031013 (2018).

[17] Y. Ma, Y. Dai, W. Wei, X. Li, and B. Huang, Phys. Chem. Chem. Phys. **16**, 17603 (2014).

[18] S.-H. Zhang and B.-G. Liu, Phys. Rev. B **100**, 165429 (2019).

[19] H. Maaß, H. Bentmann, C. Seibel, C. Tusche, S. V. Eremeev, T. R. Peixoto, O. E. Tereshchenko, K. A. Kokh, E. V. Chulkov, J. Kirschner, and F. Reinert, Nat. Commun. **7**, 11621 (2016).

[20] W.-Z. Xiao, H.-J. Luo, and L. Xu, J. Phys. D: Appl. Phys. **53**, 245301 (2020).

[21] S.-D. Guo, X.-S. Guo, Z.-Y. Liu, and Y.-N. Quan, J. Appl. Phys. **127**, 064302 (2020).

[22] S.-D. Guo, A.-X. Zhang, and H.-C. Li, Nanotechnology **28**, 445702 (2017).

[23] L. Wu, J. Yang, T. Zhang, S. Wang, P. Wei, W. Zhang, L. Chen, and J. Yang, J. Phys.: Condens. Matter **28**, 085801 (2016).

[24] Z. Kovacs-Krausz, A. M. Hoque, P. Makk, B. Szentpéteri, M. Kocsis, B. Fulop, M. V. Yakushev, T. V. Kuznetsova, O. E. Tereshchenko, K. A. Kokh *et al.*, Nano Lett. **20**, 4782 (2020).

[25] J. Jacimovic, X. Mettan, A. Pisoni, R. Gaal, S. Katrych, L. Demko, A. Akrap, L. Forró, H. Berger, P. Bugnon *et al.*, Scr. Mater. **76**, 69 (2014).

[26] M. Moroz and M. Prokhorenko, Inorg. Mater. **52**, 765 (2016).

[27] S. Li, L. Xu, X. Kong, T. Kusunose, N. Tsurumachi, and Q. Feng, J. Mater. Chem. C **8**, 3821 (2020).

[28] X. Su, G. Zhang, T. Liu, Y. Liu, J. Qin, and C. Chen, Russ. J. Inorg. Chem. **51**, 1864 (2006).

[29] D. C. Hvazdouski, M. S. Baranava, and V. R. Stempitsky, IOP Conf. Ser.: Mater. Sci. Eng. **347**, 012017 (2018).

[30] H. Shi, W. Ming, and M.-H. Du, Phys. Rev. B **93**, 104108 (2016).

[31] A. M. Ganose, K. T. Butler, A. Walsh, and D. O. Scanlon, J. Mater. Chem. A **4**, 2060 (2016).

[32] A. M. Ganose, S. Matsumoto, J. Buckeridge, and D. O. Scanlon, Chem. Mater. **30**, 3827 (2018).

[33] S.-D. Guo and H.-C. Li, Comput. Mater. Sci. **139**, 361 (2017).

[34] A. Akrap, J. Teyssier, A. Magrez, P. Bugnon, H. Berger, A. B. Kuzmenko, and D. van der Marel, Phys. Rev. B **90**, 035201 (2014).

[35] A. Makhnev, L. Nomerovannaya, T. Kuznetsova, O. Tereshchenko, and K. Kokh, Opt. Spectrosc. **121**, 364 (2016).

[36] W. Zhou, J. Lu, G. Xiang, and S. Ruan, J. Raman Spectrosc. **48**, 1783 (2017).

[37] M. Jin, S. Zhang, L. Xing, W. Li, G. Zhao, X. Wang, Y. Long, X. Li, H. Bai, C. Gu *et al.*, J. Phys. Chem. Solids **128**, 211 (2019).

[38] M.S. Bahramy, B.-J. Yang, R. Arita, and N. Nagaosa, Nat. Commun. **3**, 679 (2012).

[39] A. Ohmura, Y. Higuchi, T. Ochiai, M. Kanou, F. Ishikawa, S. Nakano, A. Nakayama, Y. Yamada, and T. Sasagawa, Phys. Rev. B **95**, 125203 (2017).

[40] S. Z. Murtaza and P. Vaqueiro, J. Solid State Chem. **291**, 121625 (2020).

[41] A. Crepaldi, L. Moreschini, G. Autès, C. Tournier-Colletta, S. Moser, N. Virk, H. Berger, P. Bugnon, Y. J. Chang, K. Kern, A. Bostwick, E. Rotenberg, O. V. Yazyev, and M. Grioni, Phys. Rev. Lett. **109**, 096803 (2012).

[42] D. Hajra, R. Sailus, M. Blei, K. Yumigeta, Y. Shen, and S. Tongay, ACS Nano **14**, 15626 (2020).

[43] G. Kresse and J. Hafner, Phys. Rev. B **47**, 558 (1993).

[44] G. Kresse and J. Hafner, Phys. Rev. B **49**, 14251 (1994).

[45] G. Kresse and J. Furthmüller, Comput. Mater. Sci. **6**, 15 (1996).

[46] G. Kresse and J. Furthmüller, Phys. Rev. B **54**, 11169 (1996).

[47] W. Kohn and L. J. Sham, Phys. Rev. **140**, A1133 (1965).

[48] P. Hohenberg and W. Kohn, Phys. Rev. **136**, B864 (1964).

[49] P. E. Blöchl, Phys. Rev. B **50**, 17953 (1994).

[50] J. P. Perdew, K. Burke, and M. Ernzerhof, Phys. Rev. Lett. **77**, 3865 (1996).

[51] H. J. Monkhorst and J. D. Pack, Phys. Rev. B **13**, 5188 (1976).

[52] M. Gmitra, S. Konschuh, C. Ertler, C. Ambrosch-Draxl, and J. Fabian, Phys. Rev. B **80**, 235431 (2009).

[53] J. Heyd, G. E. Scuseria, and M. Ernzerhof, J. Chem. Phys. **118**, 8207 (2003).

[54] A. V. Krukau, O. A. Vydrov, A. F. Izmaylov, and G. E. Scuseria, J. Chem. Phys. **125**, 224106 (2006).

[55] A. Togo and I. Tanaka, Scr. Mater. **108**, 1 (2015).

[56] M. Yagmurcukardes, F. M. Peeters, and H. Sahin, Phys. Rev. B **98**, 085431 (2018).

[57] J. Neugebauer and M. Scheffler, Phys. Rev. B **46**, 16067 (1992).

[58] G. Henkelman, A. Arnaldsson, and H. Jónsson, Comput. Mater. Sci. **36**, 354 (2006).

[59] Z. Kahraman, A. Kandemir, M. Yagmurcukardes, and H. Sahin, J. Phys. Chem. C **123**, 4549 (2019).

[60] A. Mogulkoc, Y. Mogulkoc, S. Jahangirov, and E. Durgun, J. Phys. Chem. C **123**, 29922 (2019).

[61] A. Bafekry, S. Karbasizadeh, C. Stampfl, M. Faraji, H. Do Minh, A. S. Sarsari, S. Feghhi, and M. Ghergherehchi, Phys. Chem. Chem. Phys. **23**, 15216 (2021).

[62] W. Yang, Z. Guan, H. Wang, and J. Li, Phys. Chem. Chem. Phys. **23**, 6552 (2021).

[63] A. Shevelkov, E. Dikarev, R. Shpanchenko, and B. Popovkin, J. Solid State Chem. **114**, 379 (1995).

[64] X. Zhang, Y. Guo, Z. Zhou, Y. Li, Y. Chen, and J. Wang, Energy Environ. Sci. **14**, 4059 (2021).

[65] R. Dautray and J.-L. Lions, *Mathematical Analysis and Numerical Methods for Science and Technology* (Springer Science & Business Media, Paris, 2012).

[66] E. Lifshitz, A. Kosevich, and L. Pitaevskii, *Theory of Elasticity* (Butterworth-Heinemann, Oxford, 1986).

[67] X. Gu and R. Yang, Appl. Phys. Lett. **105**, 131903 (2014).

[68] U. Argaman, R. E. Abutbul, Y. Golan, and G. Makov, Phys. Rev. B **100**, 054104 (2019).

[69] A. J. H. McGaughey, M. I. Hussein, E. S. Landry, M. Kaviany, and G. M. Hulbert, Phys. Rev. B **74**, 104304 (2006).

[70] See Supplemental Material at http://link.aps.org/supplemental/10.1103/PhysRevMaterials.5.104001 for additional details on molecular dynamics results of Janus Bi*XY* monolayers at 600 K, atomic displacements of Raman-active modes in BiSeI crystal, and orbital projected density of states (PDOS) results.

[71] M. Yagmurcukardes, C. Bacaksiz, E. Unsal, B. Akbali, R. T. Senger, and H. Sahin, Phys. Rev. B **97**, 115427 (2018).

[72] I. Y. Sklyadneva, R. Heid, K.-P. Bohnen, V. Chis, V. A. Volodin, K. A. Kokh, O. E. Tereshchenko, P. M. Echenique, and E. V. Chulkov, Phys. Rev. B **86**, 094302 (2012).

[73] M. Born and K. Huang, *Dynamical Theory of Crystal Lattices* (Clarendon Press, 1954).

[74] F. Mouhat and F.-X. Coudert, Phys. Rev. B **90**, 224104 (2014).

[75] W. Shi and Z. Wang, J. Phys.: Condens. Matter **30**, 215301 (2018).

[76] S.-D. Guo, Phys. Chem. Chem. Phys. **20**, 7236 (2018).

[77] I. Frantsevich, F. Voronov, and S. Bokuta, *Elastic Constants and Elastic Moduli of Metals and Insulators Handbook* (Naukova Dumka, Kiev, Ukraine, 1983), pp. 60–180.

[78] W. Köster and H. Franz, Metall. Rev. **6**, 1 (1961).

[79] S.-E. Park and T. R. Shrout, J. Appl. Phys. **82**, 1804 (1997).

[80] R. Hinchet, U. Khan, C. Falconi, and S.-W. Kim, Mater. Today **21**, 611 (2018).

[81] M. N. Blonsky, H. L. Zhuang, A. K. Singh, and R. G. Hennig, ACS Nano **9**, 9885 (2015).

[82] L. C. Gomes, A. Carvalho, and A. H. Castro Neto, Phys. Rev. B **92**, 214103 (2015).

[83] M. Yagmurcukardes, C. Sevik, and F. M. Peeters, Phys. Rev. B **100**, 045415 (2019).

[84] M. Yagmurcukardes and F. M. Peeters, Phys. Rev. B **101**, 155205 (2020).

[85] M. J. Varjovi, M. Yagmurcukardes, F. M. Peeters, and E. Durgun, Phys. Rev. B **103**, 195438 (2021).